RESEARCH ARTICLE | FEBRUARY 16 2017

Ultrasonic wavefield imaging: Research tool or emerging NDE method?

Jennifer E. Michaels

AIP Conf. Proc. 1806, 020001 (2017)
https://doi.org/10.1063/1.4974542

Ultrasonic Wavefield Imaging: Research Tool or Emerging NDE Method?

Jennifer E. Michaels [a)]

School of Electrical and Computer Engineering,
Georgia Institute of Technology, Atlanta, GA 30332-0250

[a)] Corresponding author: jemichaels@gatech.edu

Abstract. Ultrasonic wavefield imaging refers to acquiring full waveform data over a region of interest for waves generated by a stationary source. Although various implementations of wavefield imaging have existed for many years, the widespread availability of laser Doppler vibrometers that can acquire signals in the high kHz and low MHz range has resulted in a rapid expansion of fundamental research utilizing full wavefield data. In addition, inspection methods based upon wavefield imaging have been proposed for standalone nondestructive evaluation (NDE) with most of these methods coming from the structural health monitoring (SHM) community and based upon guided waves. If transducers are already embedded in or mounted on the structure as part of an SHM system, then a wavefield-based inspection can potentially take place with very little required disassembly. A frequently-proposed paradigm for wavefield NDE is its application as a follow-up inspection method using embedded SHM transducers as guided wave sources if the *in situ* SHM system generates an alarm. Discussed here is the broad role of wavefield imaging as it relates to ultrasonic NDE, both as a research tool and as an emerging NDE method. Examples of current research are presented based upon both guided and bulk wavefield imaging in metals and composites, drawing primarily from the author's work. Progress towards wavefield NDE is discussed in the context of defect detection and characterization capabilities, scan times, data quality, and required data analysis. Recent research efforts are summarized that can potentially enable wavefield NDE.

INTRODUCTION

Anyone who has watched the water waves resulting from an object dropped in a pond or lake can appreciate the intuitive value of wavefield imaging. Watching a "movie" of wave motion resulting from a fixed source is invaluable for understanding how waves propagate and interact with any obstacles in their path. For ultrasonic nondestructive evaluation (NDE), such insight can directly lead to improved inspection methods. An early method for observing ultrasonic waves in solids was based upon photoelastic birefringence and utilized stroboscopic lighting to visualize waves propagating in transparent solids [1,2]. The currently preferred method for acquiring wavefield data is the laser Doppler vibrometer (LDV), which is now financially within the reach of many laboratories worldwide, and numerous papers have been published on the measurement of ultrasonic waves generated by a fixed piezoelectric transducer [3-5]. More recently, completely non-contact laser-based systems have been described in which waves are generated by a fixed laser and measured by a scanned LDV. An alternative approach is to generate waves with a scanned laser and receive with either a fixed piezoelectric transducer or a fixed LDV; the waves appear to originate at the fixed receiver location due to reciprocity of transmission and reception for linear elastodynamic systems. These techniques are described and compared in [6]. Yet another relatively common means of obtaining wavefield data is the use of air-coupled transducers, which have the advantage of low cost (compared to laser equipment) and fast scan speeds, but have several disadvantages, mainly related to data quality because of the large impedance mismatch between air and the specimen under test [7,8].

Early wavefield studies were concerned primarily with effective visualization of ultrasonic wave motion and qualitative comparisons to predicted behavior such as the study reported in [9], but the focus soon shifted to quantifying propagation. Frequency-wavenumber methods as applied to wavefield data recorded along one spatial

43rd Annual Review of Progress in Quantitative Nondestructive Evaluation, Volume 36
AIP Conf. Proc. 1806, 020001-1–020001-14; doi: 10.1063/1.4974542
Published by AIP Publishing. 978-0-7354-1474-7/$30.00

dimension were first proposed in [10] to visualize dispersion curves for multi-modal Lamb wave propagation; data were obtained using contact variable-angle wedges. Both 2-D and 3-D Fourier methods have been applied to wavefield data by many researchers to both quantify propagation and filter wavefields to extract, for example, a single mode or range of propagation directions [11-13]. More recently, 3-D frequency-wavenumber filtering has been applied to bulk wave propagation to separate Rayleigh, shear and longitudinal waves [14].

Many wavefield imaging studies utilizing guided waves have noted the interaction of guided waves with various types of defects such as cracks [15], corrosion [16], and impact damage [17]. Researchers in the area of structural health monitoring (SHM), also referred to as *in situ* NDE, are proposing arrays of permanently attached transducers to continuously monitor critical structures using guided waves [18,19], and wavefield imaging has greatly contributed to the understanding of how such waves interact with damage. If such an SHM system generates an alarm, a more thorough inspection will be required. Using one or more of the attached SHM transducers as sources of guided waves for wavefield imaging has thus been proposed as a follow-up NDE method that has the desirable characteristic of being non-contact [20,21].

Although wavefield movies allow visualization of guided waves interacting with very small (compared to the wavelength) defects, it is challenging to quantify damage via C-scan-like images similar to those obtained with conventional NDE methods. Numerous papers have been published on various methodologies for quantifying damage. Early efforts considered "snapshot" visualization [22] as well as accumulated energy plots [23]. Other approaches include standing wave analysis [6], wavenumber filtering [24], instantaneous wavenumber techniques [25-27], anomaly detection via dictionary learning [28], and a combined beamforming and wavenumber analysis technique [29], although this list is certainly not inclusive.

This current paper first provides a few basics on acquisition and interpretation of wavefield data. Next, several case studies of both guided and bulk wavefield imaging are provided that relate to detection and characterization of damage. These are followed by concluding remarks that include a discussion of the status of wavefield imaging as an NDE method.

WAVEFIELD BASICS

Fundamental to wavefield acquisition is data sampling in both time and space. Temporal sampling should obey the Nyquist criterion, which states that the sampling frequency must be more than twice that of the highest frequency present in the signals. In reality, data are typically oversampled, at least in the laboratory, at five to ten times the Nyquist rate to provide a smooth representation of the signals. Since such digitizers are readily available for the ultrasonic frequency ranges typical for ultrasonic NDE and memory is relatively inexpensive, such oversampling is usually not a big burden. Such is not the case, however, for spatial sampling. To meet the spatial Nyquist criterion, the spatial sampling increment must be less than half of the smallest wavelength of propagating waves. Since the acquisition time is proportional to the number of waveforms acquired, halving the spatial sampling increment quadruples the acquisition time for an area scan. If the spatial Nyquist criterion is not met, the data may still be useful but it will likely not be possible to apply frequency-wavenumber methods.

When acquiring guided wavefields, one must be cognizant of the difference between group velocity and phase velocity, which is caused by geometric dispersion. Figure 1 shows LDV data acquired from a 1-D scan (in space) of guided waves propagating in a 2.54 mm thick aluminum plate. There are two guided wave modes present, the faster S_0 mode and the slower A_0 mode. The weaker but faster S_0 mode is largely non-dispersive with the group velocity of the wave packet traveling at essentially the same speed as the peaks and valleys, which travel at the phase velocity. The slower A_0 mode is strongly dispersive, and it can be clearly seen that the wave packet is traveling faster than the peaks and valleys; i.e., the group velocity is faster than the phase velocity.

If a 2-D fast Fourier transform (FFT) is taken of these signals, the time-space domain maps to the frequency-wavenumber domain. Figure 2 shows the frequency-wavenumber image of the signals in Figure 1 for two different time windows. In Fig. 2(a), a narrow time window is used that contains only the first arrivals. It can be seen in this figure that the trajectories of the two modes closely agree with the theoretical dispersion curves, which are superimposed on the image. A larger window is considered in Fig. 2(b), and although the dispersion curves are still evident, the presence of the edge reflections adds considerable complexity to the frequency-wavenumber map. In particular, the apparent phase velocities of edge reflections are higher than the actual phase velocities if the measurement direction is not coincident with the propagation direction.

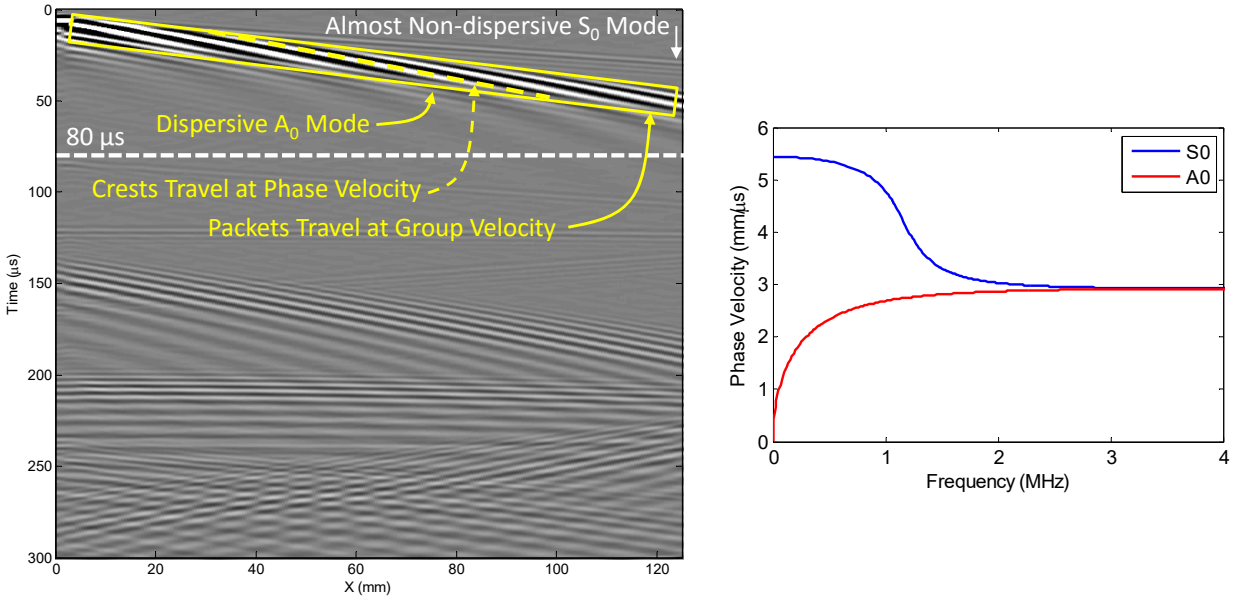

FIGURE 1. Wavefield data recorded from a 2.54 mm thick aluminum plate and the theoretical dispersion curves for the two fundamental guided wave modes.

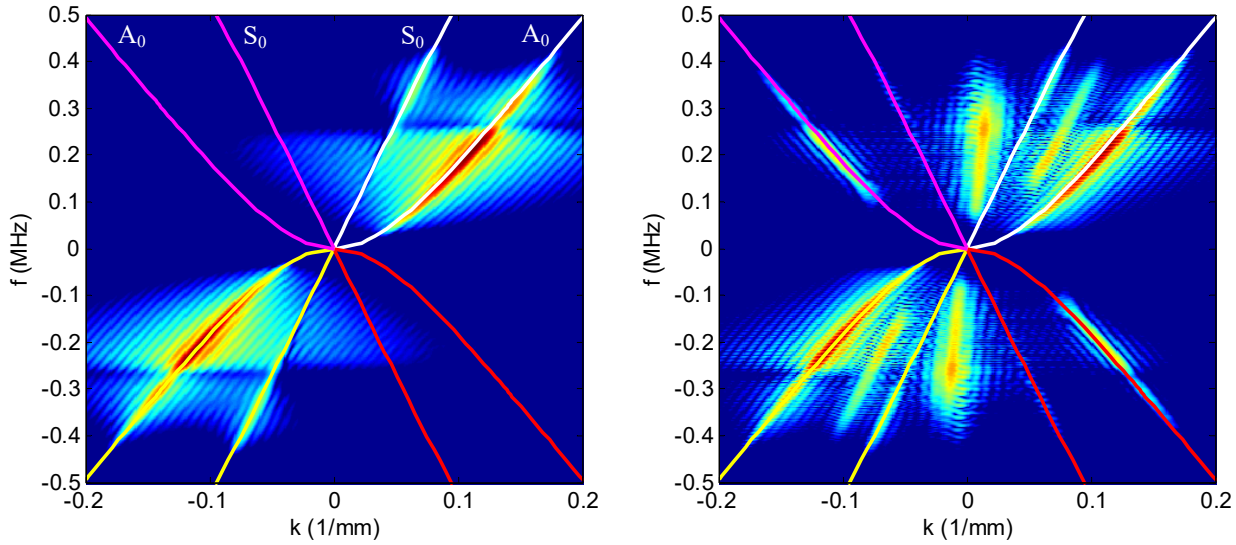

FIGURE 2. Frequency-wavenumber representation of wavefield data recorded from a 2.54 mm thick aluminum plate. (a) 80 µs window, and (b) 300 µs window.

GUIDED WAVES IN A BONDED PLATE

The first case study is that of guided waves propagating in a bonded aluminum plate [30]. The specimen was constructed by bonding together two 1.5 mm thick aluminum plates with epoxy; the bond was intentionally fabricated with numerous air bubbles and an inconsistent thickness. As seen in the sketch of Fig. 3, the upper plate, which measured approximately 355 mm × 610 mm, was twice the size of the lower plate, which measured 355 mm

× 305 mm. Four 12.5 mm diameter PZT disks were attached to the back side of the specimen, and transducer #1 was driven by an impulsive excitation to generate guided waves. The resulting wave motion was measured with a 400 kHz, 50 mm focal length, air-coupled transducer that was oriented normal to the upper specimen surface. The air-coupled transducer does not measure the wavefield directly but receives compressional waves that have "leaked" from the plate and traveled through the air gap to the receiver. The total scan time was about 20 minutes.

Figure 4 shows snapshots from the measured wavefield at four different times. The zero time reference is the time of arrival of the first wave at the receiver when the transducer is directly above the transmitter; that is, the propagation time through the air has been subtracted. In the snapshot at 50 μs, the faster, longer wavelength S_0 mode can be seen to lead the circular wavefronts followed by the slower, shorter wavelength A_0 mode. As time progresses, the waves emanating from the source transducer appear to reverberate, which is actually due to the resonance of the narrowband air-coupled receiver. The waves can be seen to interact with the other attached transducers, the vertical boundary between the single plate on the left and the double layer on the right, and the various air bubbles in the epoxy layer. In addition, mode conversion from S_0 to A_0 at both the attached transducers and the bond line can be readily observed. As time progresses, edge reflections cause the wavefield to become increasingly complicated, but also cause the epoxy layer air bubbles to become better delineated, primarily because of wave trapping within the bubbles.

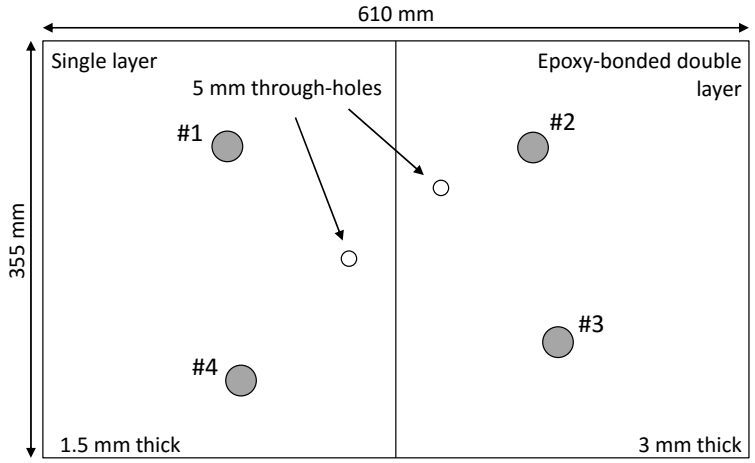

FIGURE 3. Bonded plate specimen.

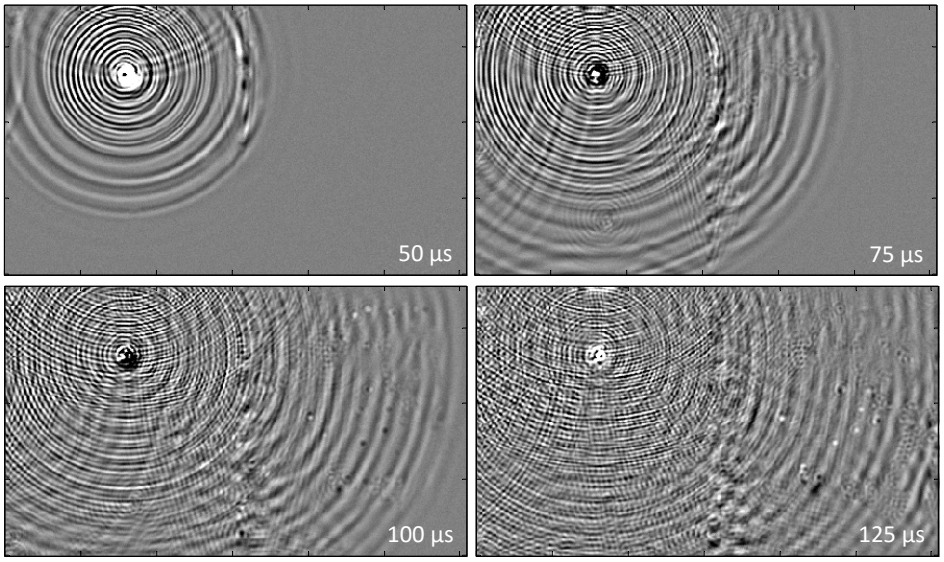

FIGURE 4. Wavefield snapshots from the bonded plate specimen.

Although the eye can readily discriminate most features of interest while playing the wavefield as a movie, it is more challenging to obtain a clear image of those features such as can be obtained by conventional ultrasonic imaging. Figure 5(a) shows a double-through-transmission C-scan of the right side of the specimen that was obtained with a 10 MHz, 12.4 mm diameter, 100 mm focal length immersion transducer. In this method, signals are generated and received in pulse-echo mode, but the gate is set to report the peak amplitude from a far-side reflecting plate. As expected, the bonding defects and the attached transducers can be clearly visualized as an almost complete loss of amplitude. Thickness variations are manifested as small changes in amplitude. Figure 5(b) shows a total energy image as obtained from the wavefield data for comparison; it might be expected that such an image would highlight energy trapping in the bonding defects. However, although there are indications in this image that correspond to the defects visible in the C-scan, it certainly does not lend itself to clear interpretation. Although not shown here, a wavefield peak amplitude image is similar to the energy image.

When viewing the wavefield movie, it can be noted that the leading edge of the faster S_0 mode has the clearest interaction with the specimen features since it is not complicated by the slower mode or any edge reflections. Although the specimen is not homogeneous, the change in wave speed of the fast mode is similar for the two halves of the bonded plate (single layer versus double layer). Thus, the arrival time t_{arr} of the fast mode at any position (x, y) on the specimen can be approximately calculated as

$$t_{\text{arr}} = \frac{\sqrt{(x - x_t)^2 + (y - y_t)^2}}{c_g}, \tag{1}$$

where (x_t, y_t) are the coordinates of the source transducer and c_g is the approximate group velocity of the fast mode. If the group velocity changed significantly from one side of the plate to the other, the arrival time could still be calculated but with a more complicated expression.

Figure 5(c) shows a gated peak amplitude image where the gate is a moving window centered at the calculated arrival time for each pixel; the window width was taken to be 15 μs and the group velocity was estimated to be 4 mm/μs. This image is remarkably similar to the through-transmission C-scan with the exception that some of the air bubbles are manifested as higher amplitude indications rather than lower.

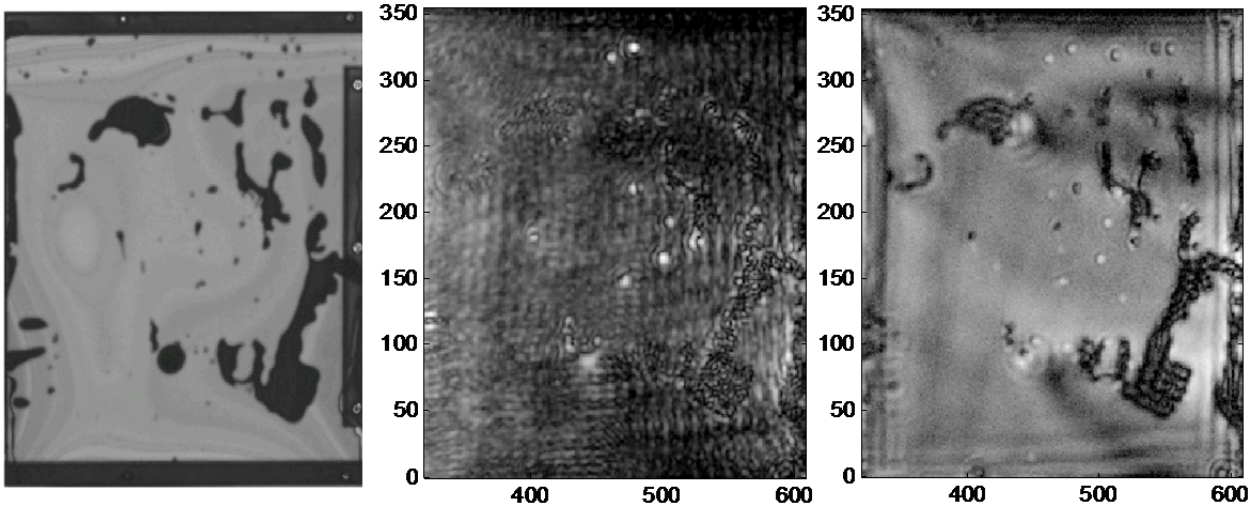

FIGURE 5. Bonded plate images. (a) Conventional double-through-transmission C-scan, (b) wavefield total energy C-scan, and (c) wavefield moving window C-scan.

GUIDED WAVES IN A COMPOSITE PLATE

The second case study considers guided waves propagating in an anisotropic composite plate with impact damage. The plate measured 460 mm × 460 mm × 2.5 mm and was nominally homogeneous with an orthotropic layup of $[0/90]_4$. It was instrumented with six PZT disk transducers, each 7 mm in diameter and with radial mode polarization and a 300 kHz resonant frequency. Impact damage was introduced in the central portion of the panel by dropping a weight, and guided waves were generated by exciting one of the transducers with a 50-500 kHz linear chirp. Wavefield data were recorded in a rectangular region surrounding the impact using a laser Doppler vibrometer (LDV) mounted on an XYZ scanner. The output of the LDV is proportional to out-of-plane displacement and is thus more sensitive to the slower A_0-like mode than the faster S_0-like mode. The spatial sampling increment in both spatial dimensions was 1.5 mm, and signals were sampled at 20 MHz. Figure 6 shows a photograph of the specimen as well as a diagram showing the scanned region and impact location. The total scan time was about six hours.

The wavefield data were post-processed to first temporally down-sample the data by a factor of four to 5 MHz, and then to deconvolve the chirp responses to yield the equivalent response to a 250 kHz, 2-cycle Hann-windowed tone burst [31]. Figure 7 shows three snapshots of the wavefield after post-processing. In the 30 µs snapshot, it can be seen that the faster mode is very anisotropic with almost square wavefronts. In the 90 µs snapshot, the slower mode has just passed the impact site and both scattering and energy trapping are evident. In the 130 µs snapshot, a reflection of the slower mode from the left edge can be seen. Although scattering from the impact site is clearly visible, the wavefield is dominated by both the incident waves and edge reflections.

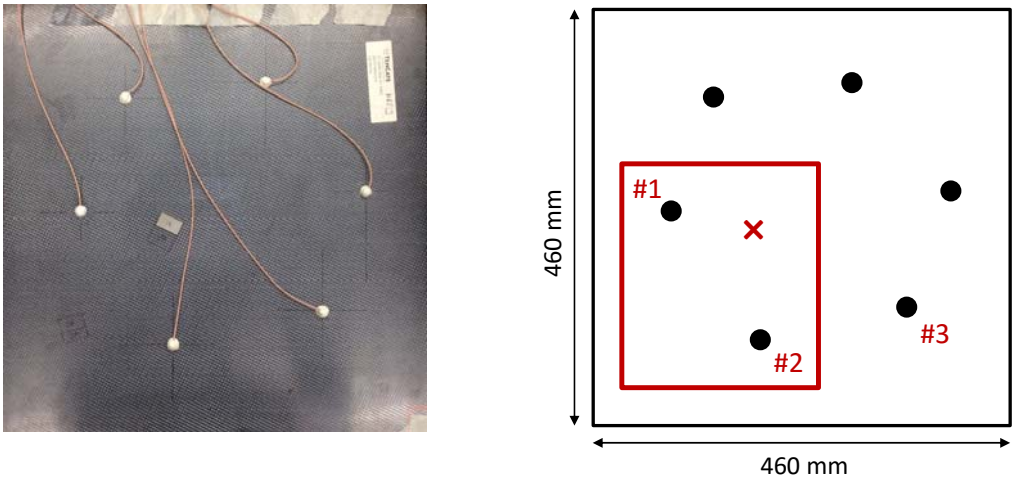

FIGURE 6. Composite panel specimen (a) photograph and (b) diagram. The box indicates the wavefield scan area and the "×" designates the impact location.

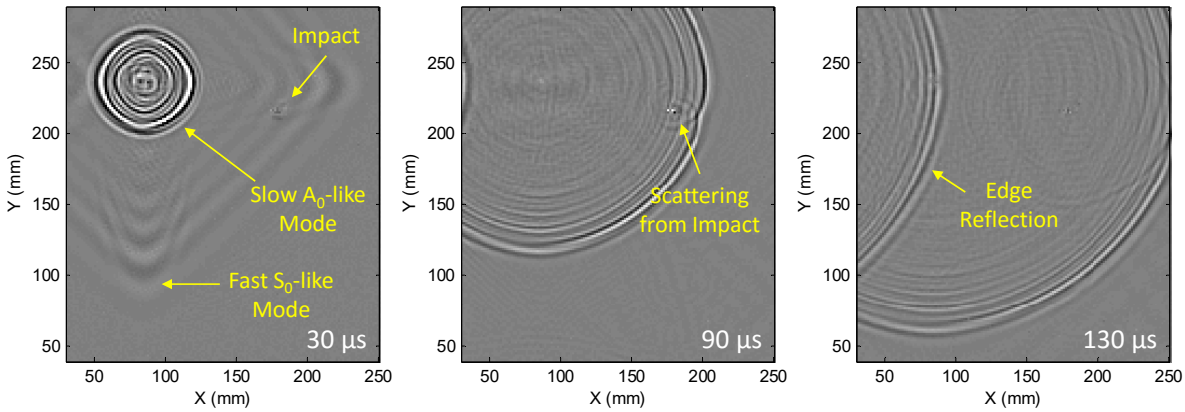

FIGURE 7. Wavefield snapshots from the composite panel specimen.

One approach for analyzing the wavefield data is to perform 1-D Fourier filtering on the time signals to examine the frequency-dependence of the scattering from impact damage. Figure 8 shows three energy images that were obtained by accumulating energy in the frequency domain corresponding to three different bands. The first considers a low-frequency band from 50-100 kHz. Although the image is dominated by the source transducer, both energy trapping and shadowing of the incident waves by the impact site are evident. The mid-frequency band image, from 150-200 kHz, is also dominated by the source but displays a larger site of energy trapping and shows more of a disturbance of the wavefield from one of the other transducers; however, there is an overall higher background noise level. The highest band image shown, from 250-300 kHz, continues the trend but it is interesting to note that the energy pattern around the source transducer has changed quite a bit. Although these frequency-domain energy images are useful, they are still not comparable to conventional C-scans in terms of their ability to unambiguously discriminate a damaged region from an undamaged one.

Another class of analysis techniques that can be brought to bear on these data are based upon multi-dimensional Fourier transforms. If a 3-D Fourier transform is applied to the entire wavefield, the data are transformed from (t, x, y) to (ω, k_x, k_y) – that is, from the 3-D time-space domain to the 3-D frequency-wavenumber domain. Figure 9 illustrates this process. Note that in the frequency-wavenumber domain, the two modes appear ring-like at each frequency with the slower mode corresponding to larger diameter rings and the faster mode lying within the slower mode ring.

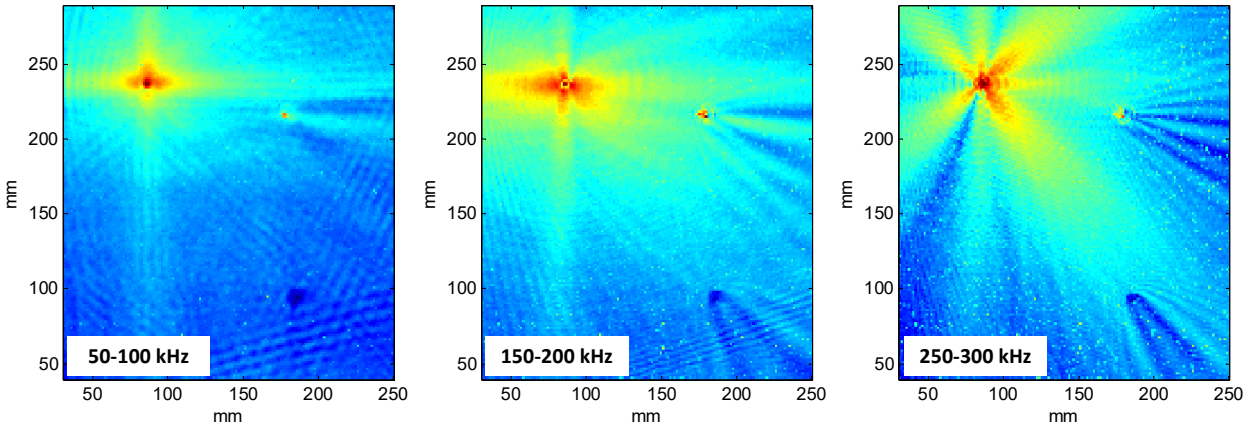

FIGURE 8. Narrowband wavefield energy images.

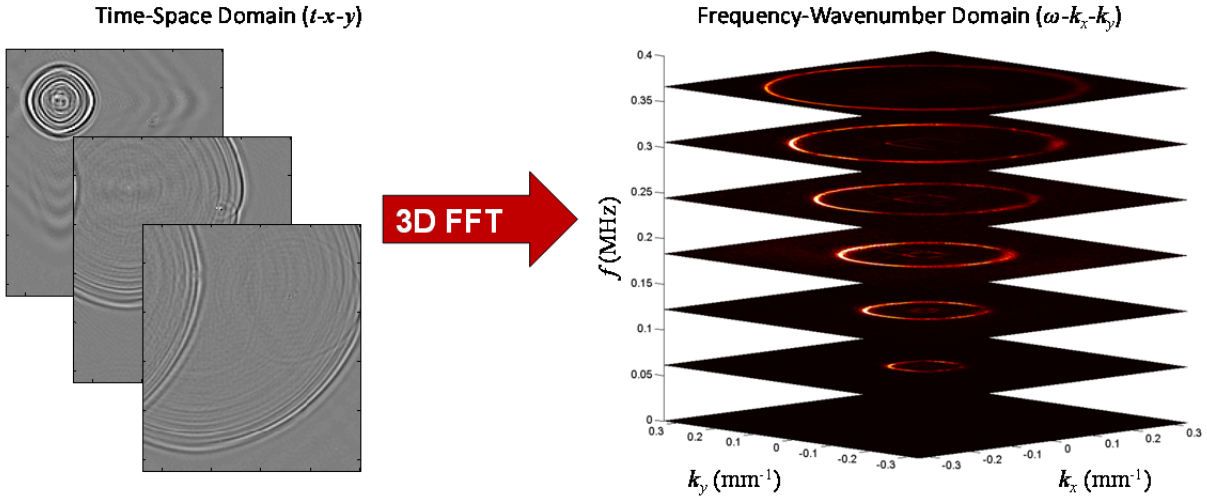

FIGURE 9. Transformation from the time-space domain to the frequency-wavenumber domain.

Extracting specific (ω, k) slices yields the more familiar dispersion curve presentation as shown in Fig. 10 for three different slices. Recalling that phase velocity $c_p = \omega/k$, we can see that the faster (weaker) mode has a steeper slope than the slower, stronger mode, and that phase velocity is a function of propagation direction. The vertical axis and the steepest white line bound the fast mode, whereas the other two white lines bound the slow mode.

Each mode can be individually extracted by applying a 3-D frequency-wavenumber filter as per these bounding lines. In addition, a third filter can be defined that extracts what is "in between" these two propagating modes. The motivation behind this third filter is any wave propagation that cannot be explained by the two well-defined propagating modes may be indicative of damage. After applying these three filters, the result is three separate wavefields – the fast S_0-like mode, the slow A_0-like mode, and what we will call "anomalous modes." Figure 11 shows energy images of these three wavefields, which confirm that the anomalous modes are indeed indicative of anomalies such as damage. The three indications on this image correspond to the two attached transducers as well as the site of impact damage, all of which are anomalies in the panel. Although not shown here, similar images were generated by exciting two of the other transducers on the panel, #2 and #3. The three images were "fused" together by averaging to yield a composite image as shown in Fig. 12(a); Fig. 12(b) shows a windowed region around the impact site. For comparison, Fig. 12(c) shows a conventional C-scan of the impact site obtained using the double-through-transmission method (i.e., pulse-echo mode but the gate is set on the echo from a reflecting plate). It can be seen that the wavefield image is comparable to the conventional C-scan.

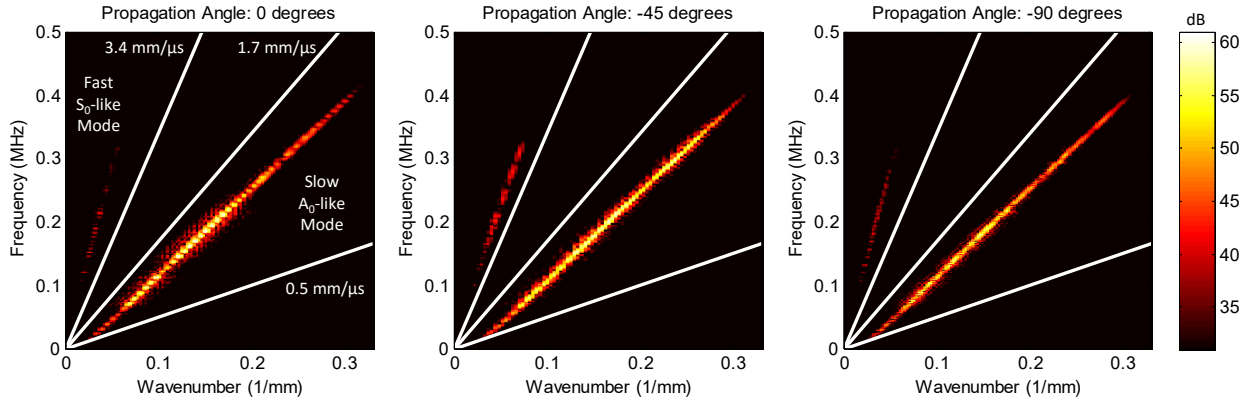

FIGURE 10. 2-D frequency-wavenumber slices extracted from the 3-D frequency-wavenumber domain.

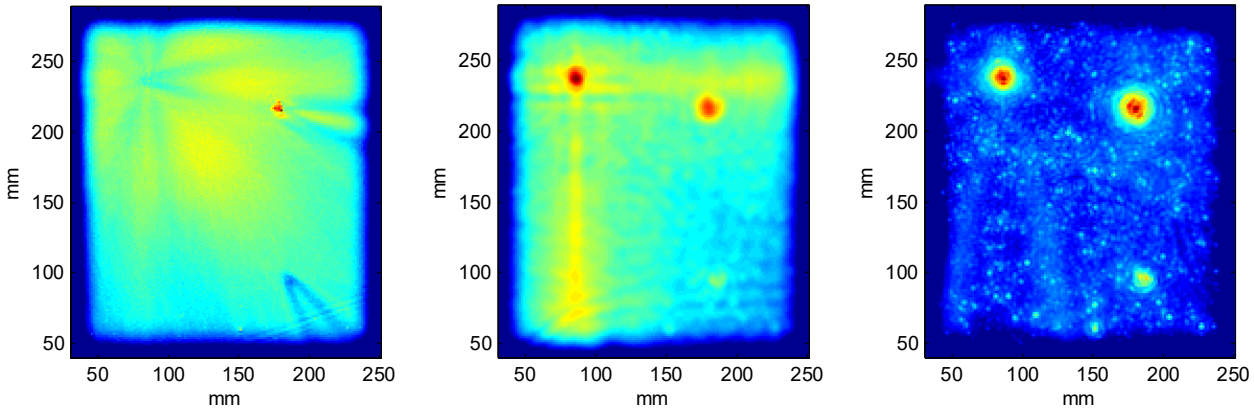

FIGURE 11. Wavefield energy images after frequency-wavenumber filtering. (a) A_0 mode, (b) S_0 mode, and (c) region in between the A_0 and S_0 modes. All images are shown on a 30 dB scale relative to the peak value.

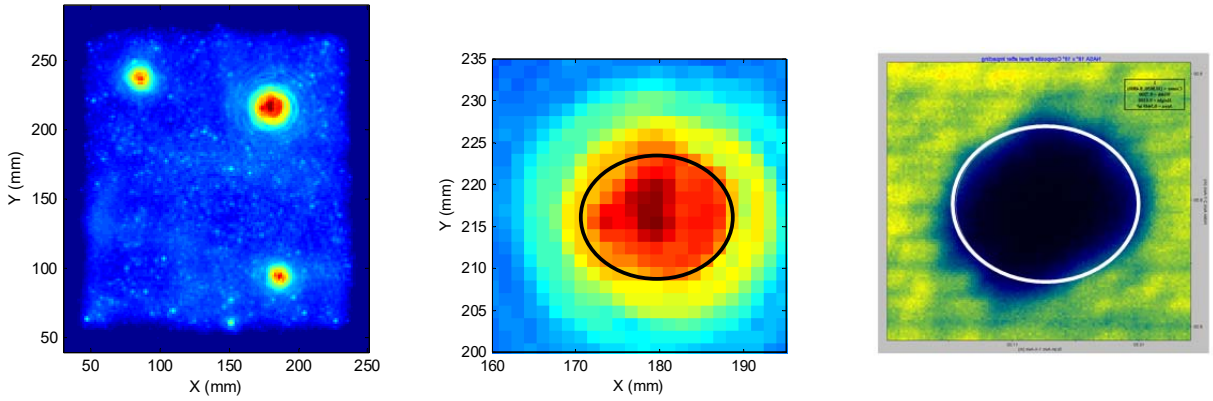

FIGURE 12. (a) Composite wavefield energy image after frequency-wavenumber filtering in the phase velocity region in between the A_0 and S_0 modes, (b) zoomed region about the impact site, and (c) conventional through-transmission C-scan. The ellipses in (b) and (c) are the same size for comparison.

BULK WAVES IN AN ALUMINUM PLATE

The third case study applies wavefield imaging to investigate scattering of angle-beam shear waves from a notch emanating from a through-hole in an aluminum plate. Although wavefield imaging is particularly suited to the measurement of guided waves, it can also be applied to bulk waves, keeping in mind that the surface measurements are only a small portion of the total wavefield.

Figure 13 illustrates the experimental configuration, in which a through-hole with a back-surface corner notch is interrogated with an angle-beam shear wave probe. Wavefield data were acquired over a 30 mm × 30 mm square region centered about the through-hole using a laser Doppler vibrometer measuring out-of-plane displacement; the total scan time was about 3.5 hours. Data sets were recorded both before and after introduction of the back-surface corner notch that was initially 1 mm in length and was subsequently enlarged to 4 mm. The transducer center frequency was 5 MHz and the nominal refracted angle was 56.8°; additional experimental details may be found in [32]. The motivation of this study is to better understand scattering of angle-beam shear waves from back surface cracks with the long term goal of improving inspection methods for such cracks.

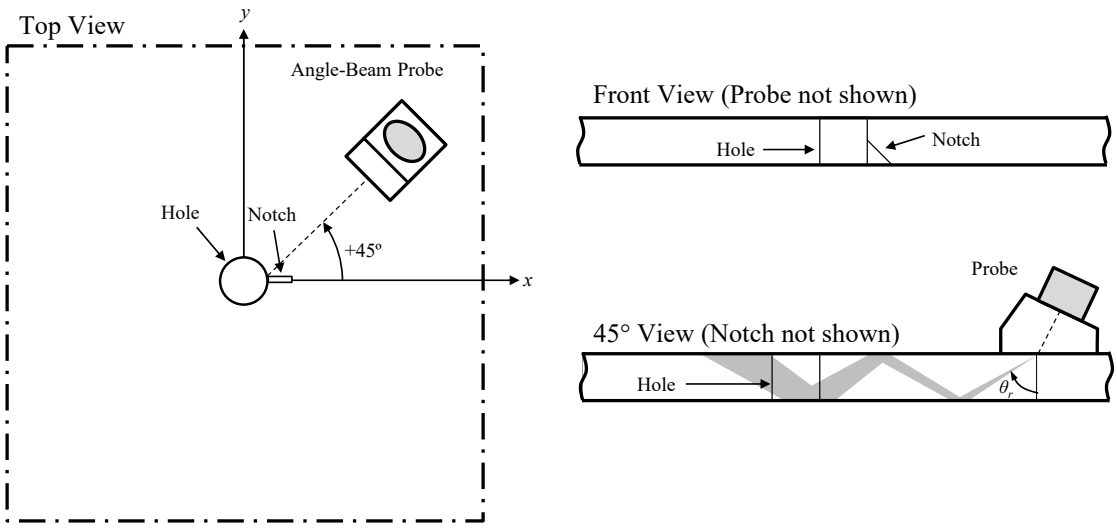

FIGURE 13. Sketch of the aluminum plate specimen showing the through-hole, back-surface corner notch, and angle-beam probe (not to scale).

Figure 14 shows three wavefield snapshots at a time of 16.88 μs from the undamaged specimen, the 2 mm notch, and the 4 mm notch. A comparison of these snapshots clearly shows scattering from the notch, and an increase in scattering for the 4 mm notch as compared to the 2 mm notch. However, the wavefields are very complicated and it is difficult to quantify the scattering from the notch by simple spatial or temporal windowing. The approach taken here generally follows that described in [14], and consists of the following steps:

- Wavefield baseline subtraction to isolate waves scattered from the notch [32]
- Frequency-wavenumber filtering in 3-D to isolate shear scattered waves from all scattered waves
- Extraction of radial B-scans to obtain scattering at different angles relative to an observation point
- Frequency-wavenumber filtering in 2-D to isolate waves propagating outward from the observation point for a specified range of phase velocities
- Accumulation of energy as a function of observation angle to generate a scattering pattern

Note that the end result captures scattered energy from all of the shear wave skips, where one skip refers to a full "bounce" from the top surface of the plate to the bottom surface and back to the top.

Figure 15 illustrates the processing steps by showing various plots for the 4 mm notch. Figure 15(a) is a snapshot of the residual signal after baseline subtraction, and although some feedthrough of the incident and hole-scattered waves are evident, it is largely successful in extracting the notch-scattered waves. Figure 15(b) shows the corresponding snapshot after 3-D frequency-wavenumber filtering to extract the shear waves. It should be noted that although the bulk shear wave speed is well-known, the apparent wave speed on the surface is faster than the bulk wave speed by a factor of $1/\sin(\theta_r)$, where θ_r is the refracted angle. Thus, the phase velocity limits for the 3-D filter were set to the nominal shear and longitudinal wave speeds of 3.11 mm/μs and 6.32 mm/μs, respectively. Setting a higher upper limit would mean that longitudinal waves could be included, which was deemed to be undesirable. Figure 15(c) shows a typical radial B-scan at an angle of −45°, and Fig. 15(d) shows its frequency-wavenumber representation. The two heavy, solid lines bracket the range of shear phase velocities (3.11 mm/μs and 6.32 mm/μs) for forward (outward) propagating waves. The thinner line at 3.72 mm/μs corresponds to the nominal refracted angle of 56.8°. It can be seen that there is very little energy outside of the shear range because of the filtering step. A point on the scattering pattern is generated by accumulating energy between two phase velocities of interest at a specific observation angle.

It is possible to generate different scattering patterns by changing the range of phase velocities. For example, Fig. 16 shows scattering patterns for the 2, 3 and 4 mm notch sizes for a narrow range of phase velocities about the nominal: 3.62 to 3.82 mm/μs (this range corresponds to a refracted angle range of 54.5° to 59.2°). These patterns all have narrow lobes with the largest lobe at about 240° (−120°), which corresponds to the notch shadowing the incident waves. All three patterns also have a strong but wider lobe at about 300° (−60°) and a third smaller lobe in the backscattered direction at close to +45°. Although the strength of all three lobes increases with notch size, their relative sizes change with the 2 mm notch having more nearly equal lobes than the 3 mm and 4 mm notches.

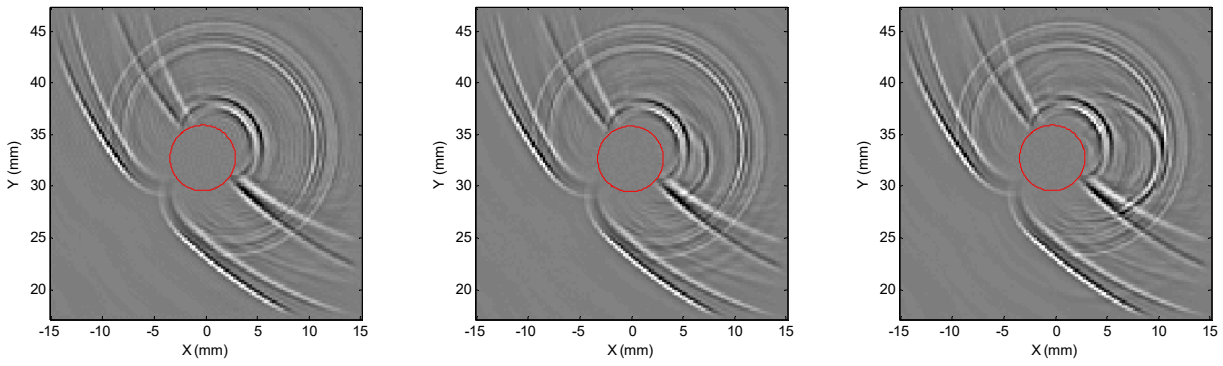

FIGURE 14. Wavefield snapshots at 16.88 μs for (a) no notch, (b) 2 mm corner notch, and (c) 4 mm corner notch.

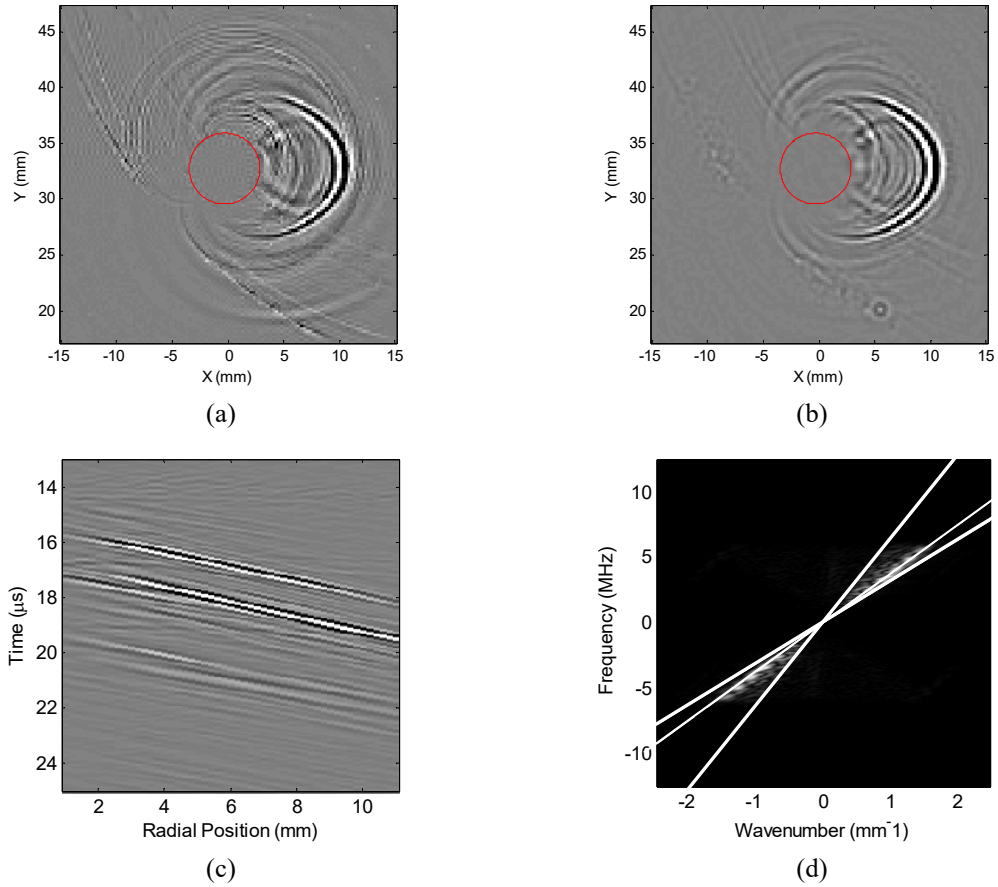

FIGURE 15. (a) Residual wavefield snapshot for the 4 mm notch at 16.88 μs, (b) residual snapshot after shear wave filtering, (c) radial B-scan at an angle of −45°, and (d) frequency-wavenumber representation of the −45° radial B-scan.

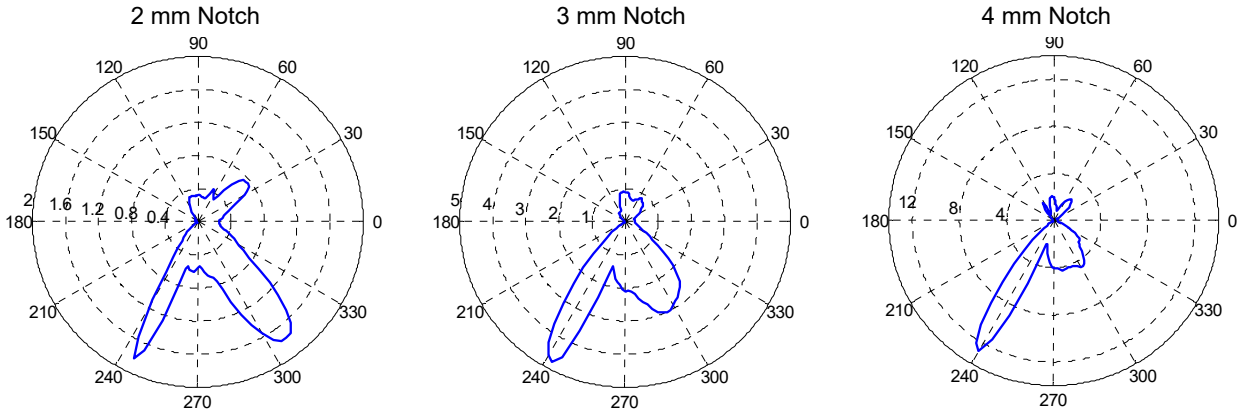

FIGURE 16. Shear scattering patterns for a narrow range of phase velocities about the nominal refracted angle.

Figure 17 shows patterns for a broader but higher range of phase velocities, 4.4 to 6.3 mm/μs, which corresponds to refracted angles of 30° to 45°. These refracted angles are not present in the incident waves, at least not to a large degree, and are likely generated via diffraction from an edge or corner. The resulting scattering patterns are not as directional as those from the narrow range of phase velocities, which is consistent with the expected more omnidirectional scattering from a sharp discontinuity.

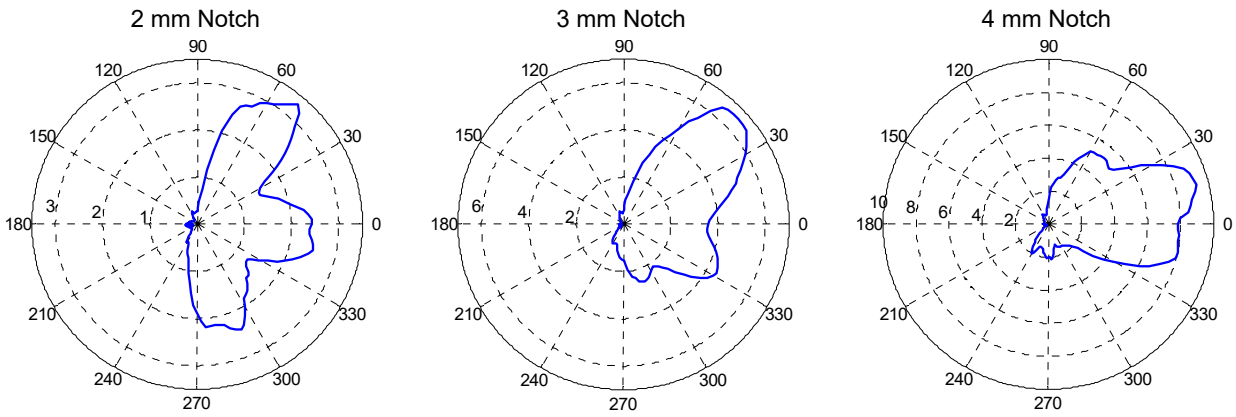

FIGURE 17. Shear scattering patterns for a range of phase velocities corresponding to refracted angles of 30° to 45°.

CONCLUDING REMARKS

There is no question that wavefield imaging is playing a critical role in understanding how ultrasonic waves propagate and interact with both damage and structural features, particularly for guided waves. But is wavefield imaging a practical and effective NDE method? Shown here are several examples of how C-scan-like images can be generated from wavefield data to effectively detect and locate discontinuities. The shear wave example further demonstrates how wavefield imaging can be used to characterize a subsurface defect by quantifying detailed scattering information. In terms of effectiveness, one can certainly argue that wavefield imaging can provide sufficient information to nondestructively evaluate a specimen for many situations of interest.

Despite this demonstrated effectiveness, the practicality of wavefield imaging still must be addressed. There are at least three closely related obstacles that must be overcome for wavefield imaging to be implemented in the field: (1) scan time, (2) data quality, and (3) data analysis methods.

In terms of scan time, acquiring good quality transient waveforms using a laser vibrometer is slow, taking as long as 1-2 seconds per data point, usually because of extensive averaging required due to poor surface conditions. Obtaining a set of data for even a modestly-sized area can thus take hours, which is prohibitive for field inspections. Using air-coupled transducers can dramatically decrease the acquisition time but at the expense of data quality [33]. Using a laser source for wave generation and a piezoelectric transducer for a receiver can also reduce the need for signal averaging and thus reduce scan times [34], but laser safety issues typically preclude this option. Recent research and development efforts are addressing this issue by considering continuous wave excitations [35,36], sparse sampling and reconstruction [37], and multi-point laser vibrometry [38].

Data quality, which is closely related to scan time, is also an issue. The quality of laser vibrometer data can always be improved by more signal averaging at the expense of scan time. Data quality is very dependent upon surface optical reflectivity, which is often improved in the laboratory by applying retro-reflective tape or reflecting paint. However, disturbing the surface removes one of the primary advantages of wavefield imaging over conventional ultrasonic NDE methods, which require couplant. Using a continuous excitation significantly improve the data quality at the frequency(ies) being excited because it is possible to inject much more energy than a pulsed excitation, but this type of excitation limits analysis options.

Ultimately the success of wavefield imaging as an NDE method will depend upon the data analysis methods. Unlike conventional ultrasonic imaging, in which both transmitter and receiver are locally scanned to map discontinuities, in wavefield imaging only the receiver is scanned and the transmitter is fixed. The presence of a defect or discontinuity affects the global wavefield, not just measurements in the vicinity of the defect. It is very challenging to extract local information from such a global disturbance, and although research efforts thus far have been moderately successful in doing so, this has been accomplished by a wide variety of methods that are application-specific.

In summary, ultrasonic wavefield imaging is perhaps the most significant experimental tool that has become available to ultrasonic researchers in recent years. Despite its importance for the development and improvement of ultrasonic NDE methods, wavefield imaging is yet not a viable NDE method for routine field inspections. The future deployment of SHM systems may be the driving force to get wavefield imaging out of the lab and into the field.

ACKNOWLEDGMENTS

The second case study was supported by Advanced Systems & Technology, Inc., Irvine, CA, as part of a NASA SBIR Phase II Award, Contract No. NNX15CL26C, Dr. Cara Leckey, program manager. The third case study was sponsored by the Air Force Research Laboratory, contract number FA8650-10-D-5210, Dr. Eric Lindgren, program manager. The author particularly appreciates the contributions of her current and former graduate students to this work—Westin Williams, Yu Weng, Carson Maki, Dr. Alexander Dawson, Joseph Kummer, and Dr. Xin Chen—as well as her colleagues, Prof. Thomas Michaels and Prof. Massimo Ruzzene.

REFERENCES

1. R. C. Wyatt, "Visualization of pulsed ultrasound using stroboscopic photoelasticity," *Non-Destructive Testing*, **5**(6), 354-358 (1972).
2. G. Hall, "Ultrasonic wave visualization as a teaching aid in non-destructive testing," *Ultrasonics*, 15(2), 57-69, (1977).
3. O. Nishizawa, T. Satoh, and X. Lei, "Detection of shear wave in ultrasonic range by using a laser Doppler vibrometer," *Review of Scientific Instruments*, **69**(6), 2572-2573 (1998).
4. M.Ruzzene, S.M. Jeong, T. E. Michaels, J. E. Michaels, and B. Mi, "Simulation and measurement of ultrasonic waves in elastic plates using laser vibrometry," *Review of Progress in Quantitative Nondestructive Evaluation*, eds, D. O. Thompson and D. E. Chimenti, (American Institute of Physics 760, Melville NY), **24**, 172-179, 2005.
5. B. Köhler and J. L. Blackshire, "Laser vibrometer study of plate waves for structural health monitoring," *Review of Progress in Quantitative Nondestructive Evaluation*, eds. D. O. Thompson and D. E. Chimenti, (American Institute of Physics 820, Melville NY), **25**, 1672-1679 (2006).
6. Y.-K. An, B. Park, and H. Sohn, "Complete noncontact laser ultrasonic imaging for automated crack visualization in a plate," *Smart Materials and Structures*, **22**, 025022(10pp) (2013).
7. M. Castaings and P. Cawley, "The generation, propagation, and detection of Lamb waves in plates using air-coupled ultrasonic transducers," *Journal of the Acoustical Society of America*, **100**(5), 3070-3077 (1996).
8. J.-R. Lee, N. Sunuwar, and C.-Y. Park, "Comparative analysis of laser ultrasonic propagation imaging system with capacitance and piezoelectric air-coupled transducers," *Journal of Intelligent Material Systems and Structures*, **25**(5), 551-562 (2014).
9. D. Algernon, B. Gräfe, F. Mielentz, B. Köhler, and F. Schubert, "Imaging of the elastic wave propagation in concrete using scanning techniques: Application for impact-echo and ultrasonic echo methods," *Journal of Nondestructive Evaluation*, eds. D.O. Thompson and D.E. Chimenti, (American Institute of Physics 975, Melville NY) **27**, 83-97 (2008).
10. D. Alleyne and P. Cawley, "A two-dimensional Fourier transform method for the measurement of propagating multimode signals," *Journal of the Acoustical Society of America*, **89**(3), 1159-1168 (1990).
11. T. Hayashi and K. Kawashima, "Single mode extraction from multiple modes of Lamb wave and its application to defect detection," *JSME International Journal*, Series A, **46**(4), 620-626 (2003).
12. M. Ruzzene, "Frequency-wavenumber domain filtering for improved damage visualization," *Smart Materials and Structures*, **16**, 2116-2129 (2007).
13. T. E. Michaels, J. E. Michaels, and M. Ruzzene, "Frequency-wavenumber domain analysis of guided wavefields," *Ultrasonics*, **51**, 452-466 (2011).
14. A. J. Dawson, J. E. Michaels, J. W. Kummer, and T. E. Michaels, "Quantification of shear wave scattering from far-surface defects via ultrasonic wavefield measurements," submitted for publication, 2016.
15. T. E. Michaels, J. E. Michaels, and M. Ruzzene, "Detection and sizing of subsurface impedance discontinuities using acoustic wavefield imaging," *Proceedings of the International Workshop on Structural Health Monitoring*, 2215-2222 (2011).
16. T. E. Michaels and J. E. Michaels, "Monitoring and characterizing corrosion in aluminum using Lamb waves and attached sensors," *Proceedings of the SPIE*, **6532**, T. Kundu, editor, 65321G(11pp) (2007).
17. H. Sohn, D. Dutta, J. Y. Yang, M. DeSimio, S. Olson, and E. Swenson, "Automated detection of delamination and disbond from wavefield images obtained using a scanning laser vibrometer," *Smart Materials and Structures*, **20**, 045017(10pp) (2011).
18. V. Giurgiutiu, A. Zagrai, and J. J. Bao, "Piezoelectric wafer embedded active sensors for aging aircraft structural health monitoring," *Structural Health Monitoring*, **1**(1), 41-61 (2002).

19. C. H. Wang, J. T. Rose, and F.-K. Chang, "A synthetic time-reversal imaging method for structural health monitoring," *Smart Materials and Structures*, **13**, 415-423 (2004).
20. T. E. Michaels and J. E. Michaels, "Integrated monitoring and inspection with attached ultrasonic transducers," *Proceedings of the SPIE*, **6177**, T. Kundu, editor, 61770E(12pp) (2006).
21. A. Gannon, E. Wheeler, K. Brown, E. Flynn, and W. Warren, "A high-speed dual-stage ultrasonic guided wave system for localization and characterization of defects," *Conference Proceedings for the Society of Experimental Mechanics Series*, **7**, 123-136 (2015).
22. J.-R. Lee, J. Takatsubo, N. Toyama, and D.-H. Kang, "Health monitoring of complex curved structures using an ultrasonic wavefield propagation imaging system," *Measurement Science and Technology*, **18**, 3816- 3824 (2007).
23. T. E. Michaels, J. E. Michaels, and M. Ruzzene, "Damage detection in plate structures using ultrasonic transducer arrays and acoustic wavefield imaging," *Review of Progress in Quantitative Nondestructive Evaluation*, **24**, D. O. Thompson and D. E. Chimenti, editors, AIP Conf. Proc. **760**, 938-945 (2005).
24. P. Kudula, M. Radzieński, and W. Ostachowicz, "Identification of cracks in thin-walled structures by means of wavenumber filtering," *Mechanical Systems and Signal Processing*, **50-51**, 456-466 (2015).
25. M. D. Rogge and C. A. C. Leckey, "Characterization of impact damage in composite laminates using guided wavefield imaging and local wavenumber domain analysis," *Ultrasonics*, **53**, 1217-1226 (2013).
26. E. B. Flynn, S. Y. Chong, G. J. Jarmer, and J.-R. Lee, "Structural imaging through local wavenumber estimation of guided waves," *NDT&E International*, **59**, 1-10 (2013).
27. O. Mesnil, C. A. C. Leckey, and M. Ruzzene, "Instantaneous and local wavenumber estimates for damage quantification in composites," *Structural Health Monitoring*, **14**(3), 193-204 (2015).
28. J. M. Druce, J. D. Haupt, and S. Gonella, "Anomaly-sensitive dictionary learning for structural diagnostics from ultrasonic wavefields," *IEEE Transactions on Ultrasonics, Ferroelectrics, and Frequency Control*, **62**(7), 1384-1396 (2015).
29. Z. Tian, L. Yu, and C. Leckey, "Rapid guided wave delamination detection and quantification in composites using global-local sensing," *Smart Materials and Structures*, **25**, 085042:1-11 (2016).
30. T. E. Michaels and J. E. Michaels, "Application of acoustic wavefield imaging to non-contact ultrasonic inspection of bonded components," *Review of Progress in Quantitative Nondestructive Evaluation*, eds. , D. O. Thompson and D. E. Chimenti, (American Institute of Physics 820, Melville NY) **25**, 1484-1491 (2006).
31. J. E. Michaels, S. J. Lee, A. J. Croxford, and P. D. Wilcox, "Chirp excitation of ultrasonic guided waves," *Ultrasonics*, **53**, p. 265-270 (2013).
32. A. J. Dawson, J. E. Michaels, and T. E. Michaels, "Isolation of ultrasonic scattering by wavefield baseline subtraction," *Mechanical Systems and Signal Processing*, **70-71**, pp. 891-903 (2016).
33. J. E. Michaels and T. E. Michaels, "On the measurement of guided wavefields via air-coupled ultrasonic transducers," *Review of Progress in Quantitative Nondestructive Evaluation*, eds. D. E. Chimenti and L.J. Bond (American Institute of Physics 1650, Melville NY) **34**, 792-798 (2005).
34. J.-R. Lee, J. Takatsubo, and N. Toyama, "Disbond monitoring at wing stringer tip based on built-in ultrasonic transducers and a pulsed laser," *Smart Materials and Structures*, **16**(4), 1025-1035 (2007).
35. E. B. Flynn, "Embedded multi-tone ultrasonic excitation and continuous scanning laser Doppler vibrometry for rapid and remote imaging of structural defects," *Proceedings of the 7th European Workshop on Structural Health Monitoring*, 1561-1567 (2014).
36. O. Mesnil, H. Yan, M. Ruzzene, K. Paynabar, and J. Shi, "Fast wavenumber measurement for accurate and automatic location and quantification of defect in composite," *Structural Health Monitoring*, **15**(2), pp. 223-234 (2016).
37. O. Mesnil and M. Ruzzene, "Sparse wavefield reconstruction and source detection using compressed sensing," *Ultrasonics*, **67**, pp. 94-104 (2016).
38. J. M. Kilpatrick and V. B. Markov, "Full-field laser vibrometer for instantaneous vibration measurement and non-destructive testing," *Key Engineering Materials*, **437**, 407-411 (2010).